Thunderstruck: Visually Simulating Electrical Storms

Jorge Alejandro Amador Herrera, Jonathan Klein, Daniel T. Banuti,
Wojtek Pałubicki, Sören Pirk, Dominik L. Michels

Fig. 1: Simulation of an intense electrical storm showcasing diverse lightning discharge types, including intra-cloud (left), cloud-to-ground (middle), and cloud-to-cloud (right) discharges, generated using our multi-physics framework. Our model captures the emergent formation lightning by coupling the processes of charge transport, cloud electrification, and bipolar discharges, all derived from a minimal set of atmospheric parameters.

Abstract—Thunderstorms are multi-physics phenomena resulting from intricate charge transfer processes in the atmosphere, which are driven by interactions between ice and water cloud particles. In this work, we present a physically-based model for simulating cloud electrification and discharge processes, enabling the simulation of emergent lightning phenomena, i.e., our approach automatically generates different types of discharges in response to dynamic atmospheric changes, relying solely on a minimal set of atmospheric parameters without requiring additional user input. We model charge separation at the microphysical level using a statistical mechanics approach to describe atmospheric electrification. Additionally, we introduce a gauge-invariant dielectric breakdown model capable of describing multiple bipolar channels, dynamic electric fields, and the electrical resistance of air, offering a comprehensive representation of lightning discharge processes. We validate our model through extensive comparisons with real data and prior state-of-the-art methods, demonstrating its capability to simulate distinct lightning types and the complete life-cycle of thunderstorms. Furthermore, we explore various applications of our framework, including real-time nowcasting, assessments in civil engineering, the generation of virtual environments featuring thunder and lightning, and the simulation of complex dielectric breakdown across diverse domains.
Supplementary Video: https://youtu.be/JCr5NY1bs34

Index Terms—Forecasting and Nowcasting, Lightning and Thunder, Numerical Simulation, Thunderstorms, Weather and Climate.

1 Introduction

The interactive and physically-plausible simulation of thunderstorms and lightning plays an important role in a number of application domains. In visual computing, this includes computer games, movies, and mixed reality applications, where realistic lightning is not only important for story telling but also to enhance the overall visual realism of scenes. Additionally, the principled simulation of thunderstorms is highly relevant for many practical applications, e.g., the arrangement of laser-guided lightning discharge protection systems [27].

Due to the intricate microphysics processes in the atmosphere and the short temporal scales involved, simulating lightning and thunder is a challenging and open research problem. In meteorology, mesoscale simulations have been widely used to study charge separation mechanisms, lightning activity over large-scale regions, and the impact of aerosols on thunderstorms [59]. In general, these approaches are designed to study specific aspects of atmospheric discharges, but they do not describe the emergence of lightning comprehensively within an integrated scheme. Moreover, frameworks used in meteorology are far from being interactive, as they usually require the use of supercomputers and specialized hardware [45]. This renders the direct application of these methods for visual computing applications infeasible. In contrast, existing methods in visual computing have primarily focused on simulating discharges within static positive potential fields [10,30,58], while relying on predefined endpoints to manually trigger and stop strikes. Similar discharge models have been developed to simulate atmospheric lightning [23,44], but they share the same limitations: requiring manual input and preprocessing for each strike, and being confined to simple positive potential field configurations. These constraints prevent such models from automatically generating diverse types of lightning strikes within a more realistic, dynamic, and bipolar atmospheric electric field.

Our contributions are as follows: (1) We develop a one-moment statistical mechanics formulation to compute charge separation resulting from water and ice particle collisions at the microphysical level. (2) We propose an extended dielectric breakdown model that incorporates gauge invariance and material resistance, enabling the description of multiple bipolar channels, electrical resistance, and dynamic electric fields. (3) We couple our cloud electrification and discharge schemes with a cloud dynamics model, generating a comprehensive simulation framework capable of simulating emergent lightning from a minimal set of canonical atmospheric parameters.

2 Related Work

The modeling and simulation of lightning and other weather phenomena is an ongoing research topic in different academic communities. While this spans a breadth of work that we cannot conclusively discuss here, we provide key pointers to the modeling and simulation of weather phenomena and lightning.

Clouds and Weather Phenomena. Kajiya and Von Herzen [29] introduced one of the first methods simulating clouds based on the underlying atmospheric phenomena. Interactive cloud simulations have been achieved by employing grid-based fluid solvers [24, 39, 42], particle-based approaches [17] and methods based on GPU-parallelization [50]. Procedural techniques for cloud modeling enable artistic control [55]. Several representations have been explored in previous contribu-

- *J.A. Amador Herrera, J. Klein, D.L. Michels are with KAUST. E-mail: {jorge.amadorherrera,jonathan.klein,dominik.michels}@kaust.edu.sa*
- *D.T. Banuti is with KIT. E-mail: danielbanuti@kit.edu*
- *W. Pałubicki is with AMU. E-mail: wp06@amu.edu.pl*
- *S. Pirk is with CAU. E-mail: sp@informatik.uni-kiel.de*

tions [4, 15, 40], also including position-based dynamics [13], layer-based approaches [54], and adaptive grid structures [47]. Apart from modeling and simulating clouds, recent work addresses other weather effects such as large-eddy phenomena [18], rain [14] and snow [16], supercells [21], complex weatherscapes [1], and cyclones [2]. The contribution of vegetation on local weather variations resulting in diverse microclimates has also been modeled to study the two-way interconnection of plant ecosystems and weather [43]. Furthermore, wildfires [34] have been simulated including flammagenitus clouds [20].

Lightning. The modeling of lightning has mostly been realized by employing physically-inspired and artistic approaches [12]. Dellera and Garbagnati [10] originally introduced a model of lightning channel progression. The first rendering-centered paper has been presented by Reed and Wyvill [48]. Kim and Lin [30] devised a physically-based lightning model that allows the lightning arch to take complex paths while dodging obstacles. Later, their model has been improved, primarily in terms of computational efficiency [32]. Yun et al. [58] developed a physically-inspired technique that is suitable for interactively placing lightnings. Lightning strikes are also hand-drawn and imported as sprites or generated following a set of procedural rules [26]. Potential-driven discharge schemes have also been coupled to mesoscale routines for simulating atmospheric lightning [23, 44].

3 Overview

The simulation of emergent lightning dynamically driven by atmospheric changes presents a significant challenge due to the intricate interplay of charge, heat, and fluid dynamics. These complex interactions govern the atmospheric electric field, which is influenced by charged water particles, including vapor, droplets, and ice. Moreover, the discharge process is an additional dynamic mechanism that facilitates rapid charge transport across different regions of the atmospheric domain. We address these challenges by proposing an integrated model tailored for the multi-physics simulation of cloud electrification and discharge, designed to balance physical complexity with user control, thus enabling the interactive exploration of a wide range of lightning phenomena.

We characterize the state of the atmosphere using six canonical variables: the wind velocity u, the mass fraction of water content q_a (including vapor q_v, cloud water q_w, cloud ice q_i, rain q_r, snow q_s, and graupel q_g) along with their associated charge Q_a, the temperature of humid air θ, and the atmospheric potential field Φ. Our framework, depicted schematically in Figure 2, is structured into three main components: (**I**) a local weather scheme for modeling heat and water continuity, (**II**) a statistical mechanics formulation for computing cloud electrification, and (**III**) a gauge-invariant discharge model describing dielectric breakdown within dynamic, bipolar electric fields.

4 Methodology

In this section, we present an overview of our physics-based model. For reference, Appendix A provides a comprehensive list of symbols, along with the corresponding values used in our simulations.

4.1 Atmospheric Model

Computing exact charge separation from collisions between water and ice particles within a cloud would require modeling every particle interaction, which is computationally unfeasible. Instead, we represent the system macroscopically using the mass fraction of particles or *hydrometeors* q_a. Statistical ensembles are then employed to infer bulk particle properties, enabling the efficient computation of charge separation while bridging microphysical interactions with large-scale cloud dynamics.

Using this macroscopic description, the dynamics of cloud formations is governed by the continuity of heat and water content during phase transitions between different hydrometeor species. There are various methods for modeling such processes. In our work, we adopt the formulation of Amador Herrera et al. [1], which effectively captures multiple cloud formations from a reduced set of atmospheric parameters. The background atmosphere is described in terms of the wind velocity u, ambient temperature T and pressure p. Then, a system of coupled transport equations is used to express the interactions between particles: snow melting into rain, vapor condensing into clouds, etc. In general, the parametrization $U_{a,b}(T,p,q_a,q_b)$ of a particle in state a transitioning to state b is a function of local temperature, pressure, and mass fractions. Using the material derivative $\mathrm{D}_t\phi = \partial\phi/\partial t + v\cdot\nabla\phi$ [35], we write the transport equations as

$$\mathrm{D}_t q_a = \sum_{j\neq a} U_{j,a} - \sum_{k\neq a} U_{a,k}\,, \tag{1}$$

where the sources $U_{j,a}$ and sinks $U_{a,k}$ represent phase transitions: e.g. $U_{s,r}$ is the fraction of snow s melting into rain r. For the exact parametrization of each transition we refer to [1].

4.2 One-Moment Electrification

Clouds acquire a net electrical charge due to the interaction between ice particles colliding inside of them, as well from capturing free ions in the atmosphere [49]. However, while ion capture has an important effect within weakly electrified clouds, the net charge in thunderstorms is mostly acquired from collisional charging between ice cloud particles [5, 6]. Consequently, we model cloud electrification through two collisional mechanisms: inductive and non-inductive.

Both charging processes, illustrated schematically in Figure 3, involve charge separation through particle collisions. Instead of modeling individual particles, our statistical scheme computes the bulk charges Q_a and Q_b for the ensembles representing the colliding particle masses q_a and q_b. To achieve this efficiently, we implement a one-moment integration approach, which enables rapid computation of net charge generation. Note that while higher-moment statistical techniques are usually applied in meteorology to study complex interactions, such as aerosol effects [53] and comparisons with specific storm event data [37], our one-moment method balances computational efficiency with accuracy, focusing on primary charge separation and electrification.

4.2.1 Statistical Ensembles

We model water and ice particles as spheres of diameter D with no internal structure. Furthermore, we assume that the number density $n_a(D)$ of particles of type a having a diameter D follows an exponential distribution:

$$n_a(D) = n_{0a}\exp\left(-D/D_a\right), \tag{2}$$

where the intercept n_{0a} is calibrated to match the experimental data of [9], and D_a is the characteristic diameter for each particle type. Then, any bulk quantity B_a can be computed by multiplying n_a with the corresponding single-particle quantity b_a and integrating over a particle ensemble of all possible diameters within a given volume. This procedure is exemplified in the supplementary material, where we compute D_a in terms of q_a, thus connecting the statistically described number density with our micro-physics scheme, and obtaining

$$D_a = \left(\frac{\rho_{\mathrm{air}} q_a}{8\pi\rho_a n_{0a}}\right)^{1/4}, \tag{3}$$

where ρ_{air} and ρ_a are the densities of air and a, respectively.

4.2.2 Non-Inductive Charging

We focus on collisions between graupel g and smaller ice particles, such as snow s and ice i, as these interactions have been identified as the primary mechanism driving non-inductive electrification [56].

Then, following our one-moment scheme, we compute the total charge transfer $\sigma_{b,g}$ from all the graupel-ice interactions[1] by integrating the charge transfer per single particle-particle collision $\sigma'_{b,g}$ over two exponentially distributed ensembles, one for b and one for graupel, which yields

$$\sigma_{b,g} = \sigma'_{b,g}\left(1 - C_{b,g}\right)\left\|v_g - v_b\right\| h_1(D_b, D_g)\,, \tag{4}$$

[1] Here, b is a dummy index standing for ice i and snow s.

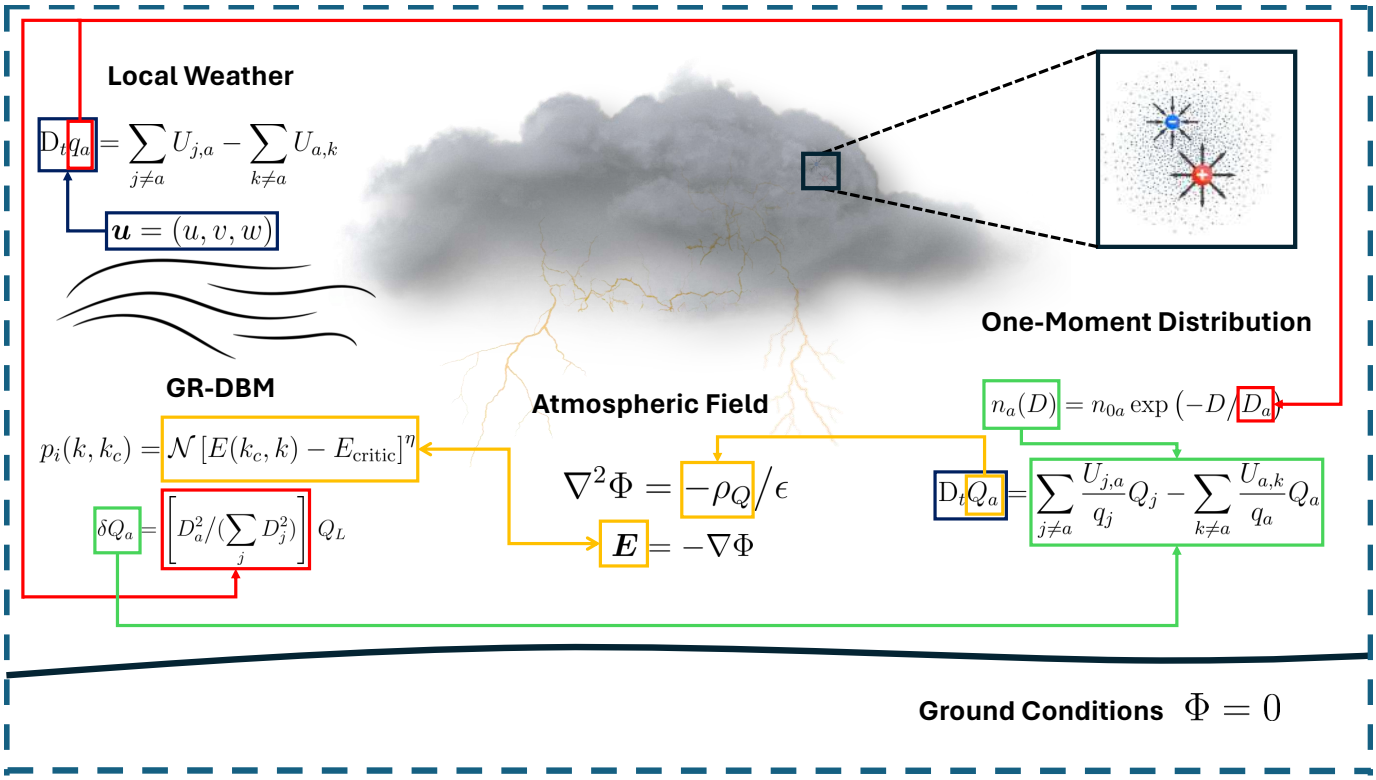

Fig. 2: Schematic representation of our "Thunderstorm" framework for simulating emergent lightning phenomena. Our integrated scheme can be divided into (**I**) a local weather model describing heat and water continuity (red) (**II**) a one-moment statistical mechanics approach for computing charge separation at the microphysical level (green), and (**III**) a discharge model describing dielectric breakdown within bipolar, dynamic electric fields (yellow).

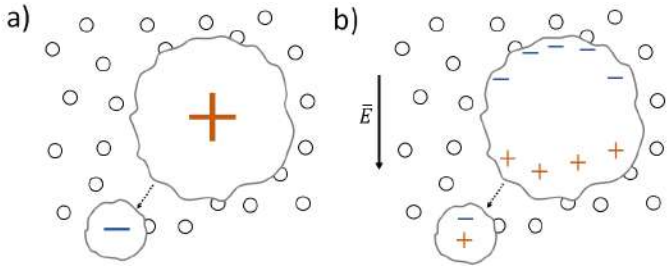

Fig. 3: Inductive and non-inductive collisional charging mechanisms: In both cases, a large graupel particle collides with a small ice or droplet while falling through the cloud droplets (small circles). Non-inductive charging (a) consists of charge being transferred via friction during the collision. In inductive charging (b), both hydrometeors are polarized by an electric field, and a fraction of their charge is neutralized during the collision, which creates a net charge difference.

where v_g and v_b are the terminal velocities of graupel and ice particles, respectively, the collection efficiency $C_{b,g}$ represents the probability of particles sticking during the collision, and $h_1(D_g, D_b)$ is given by

$$h_1(D_b, D_g) = \frac{\pi}{2} n_{0b} n_{0g} \left(D_b^2 + D_b D_g + D_g^2\right).$$

Finally, we interpolate the experimental data of Takahashi [52] to estimate the charge $\sigma'_{b,g}(\text{lwc}, T)$ transferred from b to graupel in a single collision as a function of surrounding liquid water content lwc and temperature T.

4.2.3 Inductive Charging

Falling graupel particles with a net charge generate an electric field of the opposite polarity behind them, polarizing subsequent particles and provoking a positive induction feedback. As before, we compute bulk charge transfer during inductive charging by integrating the single collision charge transfer $\tau'_{w,g}$ for graupel-water droplet interactions across two statistical ensembles, yielding

$$\tau_{w,g} = 2 v_g C_{w,g} n_{tw} n_{0g} D_w^2 \tau'_{w,g}, \tag{5}$$

with total water number density n_{tw}, and collision efficiency $C_{w,g}$. Finally, we estimate the single collision charge transfer based on the experimental findings from Ziegler et al. [60], which read

$$\tau'_{w,g} = 10.44 C_r \varepsilon E_z D_g^2 \cos(\overline{\theta}) - 0.29 Q_g / n_{tg}, \tag{6}$$

where ε is the permittivity of air, $\overline{\theta}$ is the average angle of rebounding collisions, and C_r is the rebound probability. In particular, based on the ranges of mass fraction that we encountered in our simulations, we set $C_r = 0.007$ and $\overline{\theta} = 0.2$, which correspond to the average values encountered for those mass fractions in the thunderstorm soundings of MacGorman et al. [36].

4.2.4 Net Atmospheric Field

The charge generated through collisional charging is subsequently transported and redistributed among particles via phase transitions and hydrometeor motion within the atmosphere. To capture this process, we introduce an additional set of charge transport equations, given by

$$D_t Q_a = \sum_{j\neq a} \frac{U_{j,a}}{q_j} Q_j - \sum_{k\neq a} \frac{U_{a,k}}{q_a} Q_a,$$

where Q_a is the charge being carried by a, and the source and sink terms represent the charge fraction that has been transported via phase transitions. Inductive and non-inductive charging are incorporated explicitly into the coupled system by adding the corresponding terms

into the equations for graupel g, cloud water w, cloud ice i, and snow s. Our final system is then given by

$$\mathrm{D}_t Q_g = S_g^Q + \sigma_{i,g} + \sigma_{s,g} + \tau_{w,g}\,, \tag{7}$$
$$\mathrm{D}_t Q_s = S_s^Q - \sigma_{s,g}\,,\ \mathrm{D}_t Q_i = S_i^Q - \sigma_{i,g}\,,\ \mathrm{D}_t Q_w = S_w^Q - \tau_{w,g}\,,$$

where we merged the phase-transition terms into the variable S_a^Q to keep the notation concise. Note that total charge conservation is automatically satisfied in our model, since $\sigma_{b,g} + \sigma_{g,b} = 0$ and $\tau_{w,g} + \tau_{g,w} = 0$ for non-inductive and inductive charging, respectively, and all the phase transition terms describe charge continuity. Moreover, the net charge Q_T is the sum of all the particle charge contributions, so that

$$Q_T = \sum_j Q_j\,, \tag{8}$$

where the sum iterates over all particle species. The electric potential Φ associated to this charge distribution is obtained using Poisson's equation

$$\nabla^2 \Phi = -\rho_Q/\varepsilon\,, \tag{9}$$

where ρ_Q is the volumetric charge density. Finally, the corresponding electric field is calculated as

$$E = -\nabla\Phi\,. \tag{10}$$

4.3 Lightning Discharge

Free ions in the ionosphere produce the so-called *fair weather* field $E_0 = -300\,\hat{z}\,\mathrm{V\,m^{-1}}$ [25], which grows in magnitude due to cloud electrification until it reaches the *breakdown field* $E_{\text{break}}(z)$ and is neutralized via lightning. Unlike other forms of dielectric breakdown, lightning is characterized by two oppositely charged propagation channels [46], with the discharge typically terminating within clouds or at mid-air due to the electrical resistance of the medium.

Multiple extensions of the dielectric breakdown model (DBM) by Niemeyer et al [41] have been developed to account for inhomogeneous domains [30], enhance computational efficiency [32], and improve artistic control [58]. However, all of these methods remain potential-driven schemes (PDS), as they rely on the same core growth algorithm for discharge propagation, where the probability of propagation p is given by $p \sim \Phi^\eta$, with η as a weighting factor. This formulation introduces significant limitations for simulating realistic lightning formation: negative potentials yield ill-defined probabilities, growth is indiscriminately favored in regions of positive Φ without accounting for medium resistance, and charge conservation is not enforced, leading to self-intersections, particularly in dynamic electric fields, where points within the discharge channel often satisfy $\Phi > 0$.

To address these limitations, we propose EDS: an electrical field-driven scheme that is gauge-invariant and incorporates material resistance along with multipolar channels. In the following, we outline our breakdown formulation. Moreover, a comprehensive algorithmic comparison between PDS and EDS is provided as supplemental material.

4.3.1 Stochastic Growth

Given a time-dependent field $E(x,t)$, we start the discharge at x_0 such that $||E(x_0,t) > E_b||$, where E_b is a medium-dependent *breakdown* field. The propagation of a discharge from x_0 is modeled as a step-by-step process in which we add a point to the channel by considering the magnitude of the electric field at this position in space instead of the potential. Specifically, let $\mathscr{M}$ be the set of points that are adjacent to the discharge path. We model the probability of adding $k \in \mathscr{M}$ to the channel as

$$p_i(k,k_c) = \mathscr{N}\,[E(k_c,k) - E_{\text{critic}}]^\eta \tag{11}$$

if $E(k_c,k) \geq E_{\text{critic}}$ and $p_i(k_c,k) = 0$ otherwise, where k_c is the adjacency point in the channel, $\mathscr{N}$ is a normalization constant, E_{critic} is a critical field that accounts for the electrical resistance of the discharge medium, η is a weighting factor, and $E(k_c,k)$ is the magnitude of the electric field in the direction from k_c to k. After having selected a connection pair (k_c,k_n), we add k_n to the discharge path, and update the electric potential ϕ_{k_n} at the corresponding position as

$$\Phi_{k_n} = \Phi_{k_c} - s\,d\,(k_c,k_n)\,E_{\text{int}}, \tag{12}$$

where $d\,(k_c,k_n)$ is the point distance, s is the sign of the carried polarity, and E_{int} is the internal field resistance of the channel. Finally, we update the electric potential in the rest of the domain using Poisson's Eq. (9) while treating the channel as a Dirichlet boundary condition. This process is iterated until all growth probabilities become zero.

4.3.2 Atmospheric Discharges

We parametrize a height-varying atmospheric breakdown field as

$$E_{\text{break}}(z) = 201.74\,\exp\left(-z/8.4\right), \tag{13}$$

where z is based on the thunderstorm soundings of Marshall et al. [38]. When the field at a point x_0 reaches the threshold E_b, we identify the closest adjacent point $\tilde{x}_0$ in the direction of E and start two discharge channels, one positive and one negative, that propagate from x_0 and $\tilde{x}_0$. Then, we enforce charge conservation by monitoring the total charge of each channel: when the charge magnitude of one discharge is larger than the one with opposite polarity, its propagation is stopped until the growth of the other channel compensates the charge difference. Moreover, when a channel reaches the ground, it effectively transfers charge from the atmosphere into the Earth, so we stop the propagation of the path connected to the ground and set the charge to zero on all the points in the corresponding channel, while the path of opposite polarity is allowed to grow as a unipolar discharge until it stops.

4.3.3 Charge Redistribution

When both discharge channels terminate, the charge Q_L released by lightning is redistributed into the particles in the atmosphere. In our spherical particle model, Q_L is distributed in proportion to the surface area of each particle, so the charge δQ_a gained by a is set to

$$\delta Q_a = \left[D_a^2/(\Sigma_j D_j^2)\right]\,Q_L\,, \tag{14}$$

where, for a sphere, the surface area is proportional to D_a^2, so we use the characteristic diameters directly.

ALGORITHM 1: Thunderstruck Algorithm.

Input: Current system state (u, θ, q_a, Q_a, Φ, E).
Output: Updated system state.
Procedure:
  for each $x \in \Omega$ **do**
    Update atmospheric parameters (temperature, pressure, etc.).
    Advect, diffuse, and pressure project the wind field u.
    Update microphysics processes of q_a following Eq. (1).
    Compute charge from cloud electrification according to Eqs. (4) and (5).
    Update charge continuity system given by Eq. (7).
    Sum total charge contributions as described in Eq. (8).
    Compute atmospheric potential and electric fields following Eqs. (9) and (10).
  end
  if $\|E\|$ exceeds the *breakdown field* $E_b(z)$ **then**
    Initiate lightning discharge and update electric quantities according to Algorithm 2.
    Redistribute total charge using Eq. (14).
  end
end

5 Algorithmics

In the following, we detail our numerical integration procedure, covering the discretization scheme, boundary conditions, and the numerical solver employed. Our complete *Thunderstruck* framework, as well as our EDS sub-routine, are summarized in Algorithms 1 and 2.

ALGORITHM 2: EDS Routine.

Input: Electric system (Q_a, Φ, E).
Output: Updated system state.
Procedure:
| Identify point x_A where $\|E(x_A)\| > E_b(z)$.
| Find closest adjacent point x_B in the direction of E.
| Create a negative channel starting at x_A
and a positive channel starting at x_B.
while true **do**
  for each discharge channel D **do**
    | Compute probability distribution of points $\mathscr{M}$ adjacent to D
    following Eq. (11).
    if all adjacent points have zero probability **then**
      | Finish lightning discharge.
    end
    | Sample a point $k \in \mathscr{M}$, add it to D, and update its potential
    according to Eq. (12).
    | Update the mesh potential and charge in the channel
    following Eq. (9).
    if charge conservation error is greater than 3% **then**
      | Stop the propagation of the channel with greater charge
      magnitude until the difference is below 3%.
    end
    if channel D reached the ground **then**
      | Finish lightning discharge and set its charge to 0
      due to charge transfer to the ground.
    end
  end
end while
| Redistribute charge released by lightning into hydrometeors
following Eq. (14)

5.1 Numerical Integration

We set up a staggered 3D voxel space using an uniform grid scale Δx, to store the current state of our atmospheric system: the wind field $\tilde{u}$ is stored at the faces, while the potential temperature $\tilde{\theta}$, mass fractions q_a and their associated charges Q_a, potential Φ, and electric field E are stored at the center. Moreover, we allow for non-flat ground terrains by introducing a height map $\mathscr{H} : (x_1, x_2) \rightarrow \mathscr{H}(x_1, x_2)$ such that the ground grid is embedded in the 3D space as $\partial\Omega_{\text{bottom}} = (x_1, x_2, \mathscr{H}(x_1, x_2)) \in \Omega$. Using this mesh, we discretize all the derivative operators using centered finite differences, and update the terms involving material derivatives via a semi-Lagrangian scheme, while quantities that are updated directly, e.g., charge redistribution and characteristic diameters, are computed on the fly.

Numerical integration starts by updating the atmospheric conditions, which, in our semi-Lagrangian scheme, include the advection, diffusion, and pressure projection of the wind field u, the update of temperature θ, and the transport of water described by Eq. (1). During this procedure, we set θ to the ambient temperature at the boundary, while, for all water species q_a and wind field u, we set Dirichlet boundaries at the bottom, Neumann conditions at the sides, and a free-slip boundary at the top. Afterwards, we compute the total charge from inductive and non-inductive electrification using Eqs. (4) and (5), from which we update the charge continuity system described by Eq. (7). Note that the boundary conditions for charge Q_a are the same as those for mass fractions q_a. Then, we compute the potential field generated by this charge distribution using Eq. (9), as well as the corresponding electric field by computing the numerical gradient, according to Eq. (10). We impose Neumann boundary conditions for Φ at the sides and top walls, and set $\Phi = 0$ at the ground.

Finally, if the *breakdown field* $E_b(z)$ is reached, a bipolar dielectric breakdown discharge (lightning) takes place. Since the time step sizes used for our general procedure are on the order of minutes, we consider lightning to be instantaneous.

Both the projection step of our fluid scheme and the electric potential update of EDS require the solution of a sparse Poisson problem. We use the AMGCL solver proposed by Demidov [11], which is able to efficiently solve large sparse linear systems.

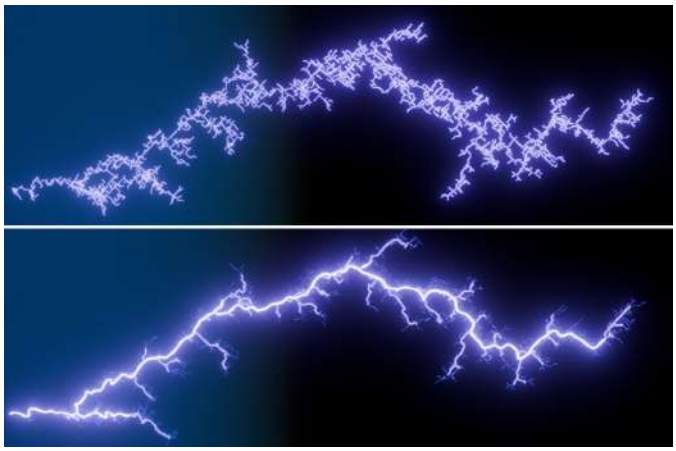

Fig. 4: Visualization of dielectric breakdown using an uniform brightness (top) and our technique (bottom). We enhance the appearance of lightning by setting the brightness proportional to the charge propagated by the channel.

Table 1: Overview of the parameters used in the scenes presented in this paper. Parameters are listed in $[T_G] = 1°\text{C}$, $[q_{gr}] = 1\,\text{kg}\,\text{kg}^{-1}$, $[E_{\text{int}}] = 1\,\text{kV}\,\text{m}^{-1}$, $[E_{\text{critic}}] = 1\,\text{kV}\,\text{m}^{-1}$, and $[\Delta t] = 1\,\text{min}$. Resolution (**R**) and runtime (**T**) in seconds per frame are listed.

Fig.	Scene	T_G	$\bar{q}_{gr}$	Δt	E_{int}	E_{critic}	R	T
1	Electrical Storm	6	0.81	5	50.0	$E_b(z)$	128^3	0.07
5	Electrification	10	0.81	5	50.0	$E_b(z)$	128^3	0.07
6	Discharge Schemes	22	0.85	5	50.0	$E_b(z)$	128^3	0.08
11	H.P. Cumulonimbus	23	0.88	5	50.0	$E_b(z)$	$128 \times 228 \times 128$	0.09
14	SEET Thunderstorm	-	-	5	50.0	$E_b(z)$	$128 \times 228 \times 128$	0.10
8	Parameter Space	18	0.83	5	50.0	$E_b(z)$	128^3	0.06
9	Multi-Layer	19	0.53	5	50.0	$E_b(z)$	228^3	0.11
15	CG	20	0.82	5	50.0	$E_b(z)$	128^3	0.04
15	IC	22	0.95	8	50.0	$E_b(z)$	228^3	0.14
15	CC	22	0.85	6	50.0	$E_b(z)$	228^3	0.13
15	CA	15	0.80	3	50.0	$E_b(z)$	128^3	0.03
15	*Bolt from the blue*	23	0.89	3	50.0	$E_b(z)$	$512 \times 256 \times 512$	0.16
15	*Anvil-Crawler*	15	0.90	2	50.0	$E_b(z)$	$512 \times 128 \times 512$	0.15
16	Cerro de la Silla	–	–	5	50.0	$E_b(z)$	$228 \times 128 \times 228$	0.10
17	Lightning Conductor	5	0.85	6	50.0	$E_b(z)$	$256 \times 128 \times 256$	0.09

5.2 Two-Grid Scheme

In order to increase the visual quality of lightning, we implement a secondary grid Ω' with $2x$ resolution for EDS computations, and use trilinear interpolation to transfer variable values from the atmospheric grid Ω into Ω'. We found that the impact on performance using this approach is negligible. Moreover, using an adaptive grid similar to Kim and Lin [32] would enable higher resolutions.

5.3 Channel Intensity

In general, the luminosity and apparent width of lightning decreases from the initiation point and main discharge path to the periphery because there is an increased flow of charge through the main part of the channel [8]. We reproduce this in our framework by setting the brightness B_L of each strike to be proportional to the charge propagated by the channel. Specifically, after the discharge, we use Poisson's equation to compute the charge distribution ρ_L of the channel from its potential. Note that this process is inverse to solving for the potential, and it only requires the computation of the Laplacian, which can be performed efficiently using finite differences. Then, we simply set $B_L = \alpha_L \rho_L$, where α_L is a proportionality constant to enable artistic control over the brightness while preserving a physically plausible visualization of the discharge channel. In Figure 4 we show an example of our technique for lightning visualization compared to a visualization without varying channel intensity.

6 Results

In this section, we present a variety of results simulated with our C++/CUDA framework, implemented as described in the previous section. Table 1 provides an overview of the different scenes presented throughout this section, including relevant parameters. Computation times listed in Table 1 are measured using an NVIDIA®GTX 3080 Ti, with double precision floating point arithmetic.

6.1 Model Evaluation

First, we performed diverse experiments to evaluate both the individual components of our model as well as our overall framework, focusing on direct comparisons to previous state-of-the-art.

6.1.1 Cloud Electrification

As shown in Figure 5, we assess our charging scheme by simulating an electrical storm using both our electrification model and prescribed potential conditions, as employed in previous works [23, 31, 33, 44, 57, 58]. The prescribed potential approach fails to capture different discharge types, such as cloud-to-air (CA) and cloud-to-cloud (CC), due to its reliance on pre-defined conditions and manual triggering for each strike. Moreover, such methods require specifying static charge arrays, initiation points, charge locations, magnitudes, and triggering times for each individual strike, which significantly increases modeling effort and makes simulating dynamic scenes with tens or even hundreds of strikes impractical. In contrast, our cloud electrification model automatically simulates the emergence of various lightning types as the environment evolves, eliminating the need for manual input and allowing for more scalable and realistic simulations.

Fig. 5: Electrical storm simulated with prescribed charges (top) and dynamic cloud electrification (bottom). Previous methods require manual definitions for each strike, including static charge arrays, initiation points, charge locations, magnitudes, and triggering times, which significantly increases the modeling effort. In contrast, our cloud electrification model automatically captures the emergence of various lightning types (from left to right: cloud-to-ground, cloud-to-air, and cloud-to-cloud) driven by dynamic environmental changes.

6.1.2 Breakdown Model

Next, we evaluate our discharge model by simulating CG and intracloud (IC) lightning using both PDS and our approach, as shown in Figure 6. The unipolar, zero-resistance and gauge constraints in PDS lead to incomplete CG strikes, with no channels propagating through the cloud, since the growth probability becomes negative as $\Phi < 0$. There is also significant overgrowth beneath the cloud as channels propagate toward all positive potential regions, ignoring the electrical resistance of the medium, which leads to an overestimation of channel extension. Additionally, IC discharges become trapped at local maxima of the potential field. In contrast, our model successfully captures both lightning types.

Furthermore, Figure 7 demonstrates that PDS requires pre-processing of the potential field to prevent regions of negative probabilities, which would cause growth algorithm to fail. Our scheme, however, consistently generates non-negative probability distributions for arbitrary fields and multiple channel polarities. Note that, for an evolving electrical field, pre-processing in PDS must be performed per-frame, as negative potential regions change over time, rendering it impractical for dynamic simulations.

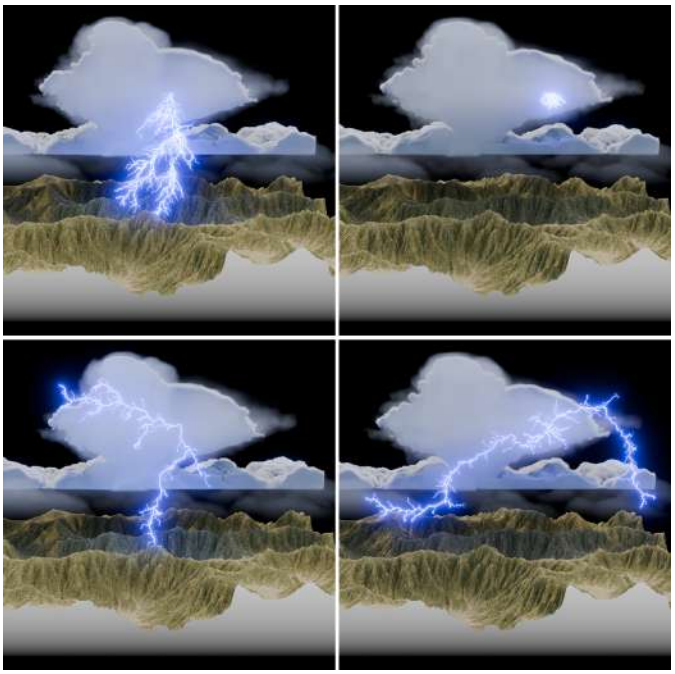

Fig. 6: Cloud-to-ground and intracloud lightning simulations shown in a cloud cross-section, using PDS (top) and EDS (bottom). In PDS, CG strikes present no growth inside the cloud and overgrowth below it (left), while IC discharges become trapped at local maxima of the potential (right). In contrast, EDS simulates realistic lightning types for the same electric field conditions.

6.1.3 Integrated System

Finally, we assess the overall behavior of our fully integrated system by conducting a parameter space exploration. As shown in Figure 8, we analyze the impact of graupel content q_g and collection efficiency $C_{b,g}$ on the average lightning activity within a storm at a fixed altitude.

Although our model incorporates numerous fixed parameters (e.g., breakdown field, hydrometeor intercepts, etc.) to ensure physical consistency, graupel content and collection efficiency provide intuitive and effective controls over thunderstorm activity.

Moreover, since clouds at higher altitudes contain a greater concentration of ice particles, lightning activity can also be influenced by adjusting relative humidity and temperature. These adjustments control storm altitude and, indirectly, the total ice fraction, enabling the simulation of complex, multi-layered thunderstorm formations such as cirrocumulus and nimbostratus clouds, as illustrated in Figure 9.

To quantitatively evaluate our framework, we performed simulations of thunderstorms with increasing ice fractions and measured the resulting lightning activity within the simulation domain. The results, shown in Figure 10, demonstrate that our framework captures the correlation between these parameters, consistent with the modified gamma function identified in the extensive analysis by Han et al. [22] using data collected by the Optical Transient Detector (OTD) and Lightning Imaging Sensor (LIS) instruments.

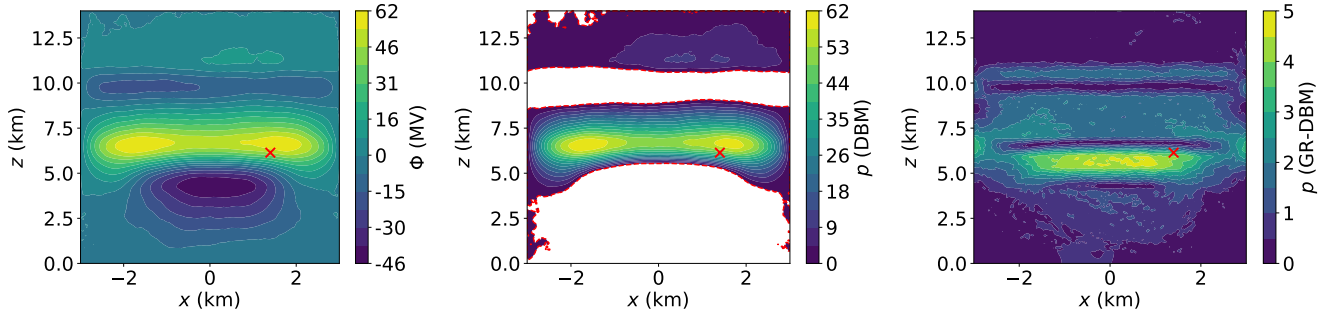

Fig. 7: Cross section (left) of the potential field of the storm shown in Figure 6 at $t \approx 3.2$ hr, and the corresponding (non-normalized) probability distributions computed using PDS (middle) and EDS (right). For a discharge triggered at the core of the storm (red marker), a substantial portion of the propagation domain corresponds to negative probabilities in PDS (blank spaces), while our scheme always produces non-negative distributions. The potential gauge must be adjusted per-frame in PDS to avoid negative probabilities, but this is not always guaranteed to work, as demonstrated in the supplemental material.

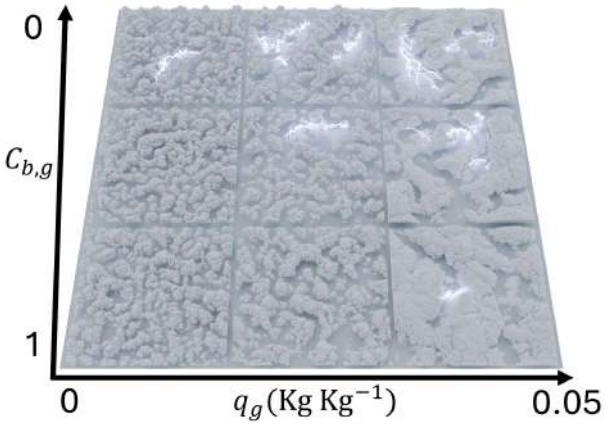

Fig. 8: Parameter space exploration showing the dependence of lightning activity on graupel mixing ratio q_g and collection efficiency $C_{b,g}$. With increased graupel content and collection efficiency the likelihood of lightning formation increases.

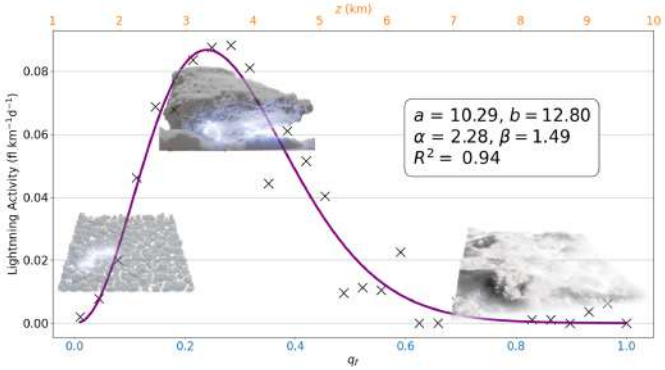

Fig. 10: Average lightning activity in clouds of increasing ice fractions. We show our simulation results (black markers), the fitted modified gamma function $L(q_f) = aq_f^{\alpha} \exp\left(-bq_f^{\beta}\right)$ (purple) with the corresponding optimum parameters, and representative clouds for each region of the plot. Our framework is able to capture the functional form of the correlation between ice fraction and lightning activity [22]

.

Fig. 9: Simulation of a multi-layered cirrocumulus and nimbostratus cloud system. As the cirrocumulus contain mostly graupel particles but no water or smaller ice crystals, there is little charge separation and almost no lightning activity. However, the nimbostratus cloud contains a large concentration of both graupel and smaller particles, which enhances cloud electrification and, thus, lightning activity.

6.2 Validation Experiments

We evaluate the validity of our approach through a series of qualitative and quantitative comparison experiments with real thunderstorm data.

6.2.1 Storm Life-Cycle

As shown in Figure 11, our multi-physics framework effectively simulates the various stages of a thunderstorm within a high-precipitation cumulonimbus cloud, capturing its development, maturation, and dissipation. By setting the temperature, pressure, and wind conditions that define the cumulonimbus, lightning emerges naturally as a result of cloud electrification and the bipolar breakdown of the surrounding air, without requiring any additional user input. This is demonstrated quantitatively in Figure 12.

6.2.2 Historical Storm

We integrated temperature, humidity, and wind velocity profiles from the SEET measurements [7], obtained through weather balloons and meteorological radars, of a historic thunderstorm into our simulation framework to virtually reconstruct the storm event, as shown in Figure 14. The intensity of inductive and non-inductive charging was then measured for three storm intensities, classified based on their temperature and graupel content profiles, and quantitatively compared to the analysis conducted by [51] using the same dataset, as shown in Figure 13. The agreement between our results and those of the previ-

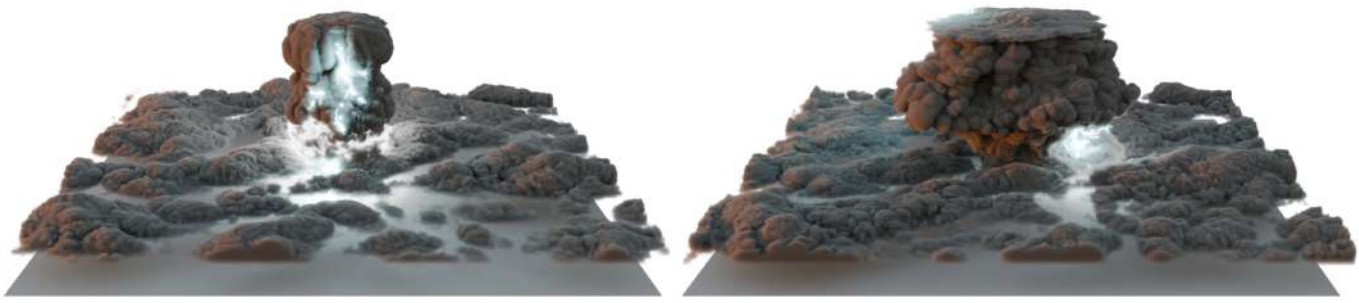

Fig. 11: Two visualizations from a high-precipitation cumulonimbus cloud simulation, captured at different stages during the storm evolution, showcasing significant lightning activity.

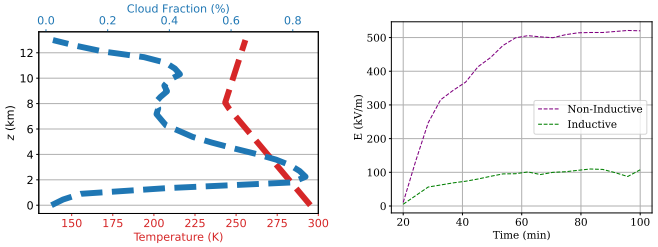

Fig. 12: Atmospheric profiles of temperature and cloud fraction (left) used in our framework to simulate a high-precipitation cumulonimbus cloud. As the storm evolves, charge separation at the microphysical level generates an increasing electric field (right), leading to the emergence of lightning without the need for predefined initiation points or charge arrays.

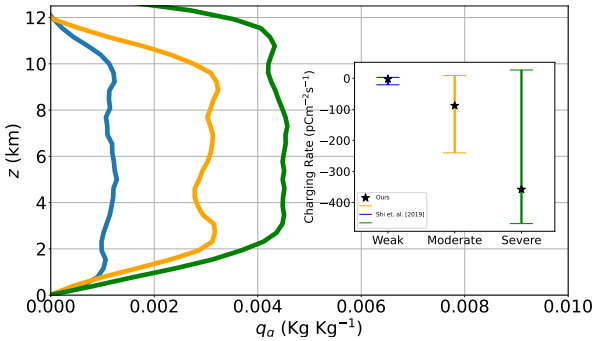

Fig. 13: We simulate three variants of the SEET storm event: weak, moderate, and severe, based on the overall storm graupel content (color plots). Then, we measure the average charging rate in each case, and compare our results to the extensive studies of [51]. Our framework produces electrification rates that lie within the value ranges obtained from highly specialized schemes.

ous study emphasizes the robustness of our framework in accurately reproducing real-world thunderstorm phenomena.

6.2.3 Lightning Types

In Figure 15 we demonstrate the capabilities of our framework to generate diverse types of atmospheric lightning that result from the complex interplay of microphysical dynamics, cloud electrification, and bipolar breakdown: (a) Cloud-to-ground lightning typically occurs when a mature thunderstorm has developed a tripole structure due to charge separation of ice particles, and one leader of the discharge path reaches the ground or a structure above it. (b) The most common type of atmospheric discharge is intracloud lightning, which consists of a bipolar channel that develops entirely within the cloud formation, connecting regions of distinct charge polarities, and generating flashes that illuminate the interior of the cloud. (c) When charge separation forms differentially charged regions on clouds at different altitudes, cloud-to-cloud lightning occurs, which travels from one cloud into another. (d) Due to the stochastic nature of dielectric breakdown, some intra-cloud discharges travel outside of the cloud and stop in mid-air, forming cloud-to-air channels, which can be encountered more often at the base of clouds. (e) In extensive cloud formations that cover greater regions, lightning that generates in one region can travel horizontally and reach a section of the cloud that has minimal charge separation, resulting in a *bolt from the blue* discharge. (f) When the storm has a precipitation core that spans large regions, CA discharges at the base of the cloud can travel great horizontal distances, generating so-called *anvil-crawlers*.

6.3 Applications

Finally, we present several use cases of our framework, including scientific and engineering applications, as well as artistic endeavors.

Fig. 14: Simulation of a real thunderstorm event based on the SEET measurements of [7] using meteorological radars. Our framework is capable of reproducing the intense lightning activity that results from the given humidity, temperature, and wind conditions.

Fig. 15: Diverse types of lightning simulated using our framework, including photo comparisons. From left to right, top to bottom: Cloud-to-ground, intracloud, cloud-to-cloud, cloud-to-air, *bolt from the blue*, and *anvil-crawler*.

6.3.1 Weather Nowcasting

We streamed atmospheric profiles of wind speed, humidity, and temperature from different weather services[2] into our solver to simulate a thunderstorm formation in real-time, enabling a combination of forecasting and nowcasting. In Figure 16, we show the result of such a simulation for the Cerro de la Silla, within the metropolitan area of Monterrey, in northeastern Mexico on April 25, 2022 starting at 0:00h local time. Our framework can provide an immersive experience for exploring real thunderstorm events virtually.

Fig. 16: We enable a nowcasting application by streaming different atmospheric profiles into our framework to simulate thunderstorms in real-time. In this example, we simulate the development of the storm at the Cerro de la Silla on april 25, 2022.

6.3.2 Lightning Conductors

We use our framework to measure the effectiveness of a lightning conductor by simulating a thunderstorm with high lightning activity in a domain with a lightning conductor mounted at the center. Our simulation is illustrated in Figure 17, while a quantitative comparison to the methodology used in [28] is shown in Figure 18. The results obtained with our model are comparable to those computed using specialized approaches.

6.3.3 Thunderstorm

The different physical mechanisms that we take into account in our model enable us to measure multiple atmospheric and discharge variables that can be used as input for subsequent models and applications. For instance, we input the time-series of the atmospheric state

[2]https://www.globalsolaratlas.info/ and https://www.ventusky.com/

Fig. 17: Simulation of a storm with intense electrical activity in a domain with a lightning conductor mounted at the center of the grid.

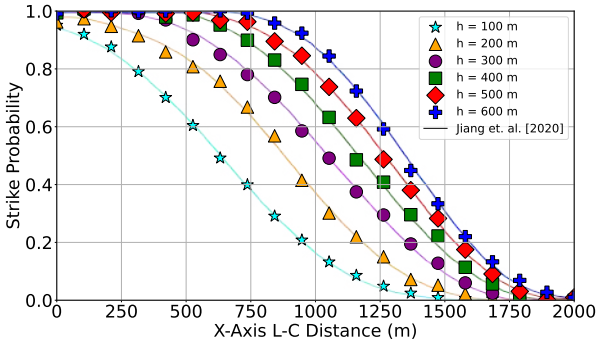

Fig. 18: Probability that a CG discharge will hit the lightning conductor in the simulation shown at 17. We measure the probability for increasing x distances between the initiation point and the conductor, as well as for increasing conductor heights h. We compare our results (markers) with the simulations of [28] (solid curves).

$A_S = (u, \theta, q_a, Q_a, \Phi, E)$ produced by our framework into an approximative acoustic model to generate a thunder simulation, as shown in the supplemental video. The parametrization of our acoustic model is included as supplemental material.

6.3.4 Complex Discharges

The primary motivation of our approach is to achieve a realistic modeling and simulation of emergent lightning phenomena. In this sense, we proposed EDS to generate discharge channels under realistic atmospheric conditions, including dynamic electric fields, multiple polarities with total charge preservation through gauge invariance, and the consideration of air and channel resistance. However, such conditions are not limited to lightning but also arise in other complex breakdown systems, where EDS can enhance the visual simulation of discharges. Several examples illustrating this capability are provided as supplemental material.

7 Discussion

We have assessed the necessity of our cloud electrification scheme, discharge model, and integrated framework for producing consistent and realistic lightning phenomena within a dynamic domain, where environmental conditions evolve significantly over time. The evaluations in Section 6.1 demonstrate that simulating lightning cannot be achieved simply by connecting the output from a cloud solver as input for an existing discharge scheme. Instead, it is essential to account for the underlying physical mechanisms that generate a dynamic atmospheric electrical field, as well as the rapid transport of charge (lightning) driven by the electric field itself, rather than relying solely on a hypothetical positive potential. Addressing these factors is crucial for ensuring a robust and accurate simulation.

Through extensive validation experiments, we have demonstrated the ability of our model to realistically simulate a wide range of discharge phenomena, including the emergence of atmospheric lightning driven by cloud electrification and the dielectric breakdown of air. We employ a statistical mechanics approach to model charge separation within clouds at the microphysical level, calculating one-moment averages for particle ensembles in the atmosphere. This approach allows us to accurately capture the influence of key factors such as ice content, cloud altitude, and collection efficiency on the overall lightning activity of a storm, as illustrated in Figures 10-13. Furthermore, our discharge model, EDS, effectively simulates complex dielectric breakdown processes, incorporating features such as bipolar branching channels, dynamic electric fields, and the electrical resistance of both the medium and the channels. This capability enables the generation of diverse lightning phenomena without requiring additional user input or preprocessing, in contrast to potential-driven methods, as illustrated in Figure 5.

Our framework captures the interplay of fluid-mechanics, thermodynamics, and electrodynamic processes to simulate the life cycle of thunderstorms and the emergent formation of lightning (Figure 11). It also allows us to reproduce diverse types of complex atmospheric lightning, as shown in Figure 15. Our integrated multi-physics approach can be used in multiple applications, including weather nowcasting (Figure 16), measuring protection zones generated by lightning conductors (Figure 17), and producing a virtual thunderstorm that can be explored interactively, including acoustic effects, as shown in the supplemental video.

Furthermore, while our main motivation is the comprehensive simulation of atmospheric lightning, our discharge scheme EDS can be applied to simulate breakdowns within other complex domains, including dielectric materials, dynamic fields produced between charged diodes and in *plasma balls*, and labyrinth-like spaces, as shown in supplemental material.

Finally, our visually realistic simulations of electric thunderstorms can serve as a synthetic dataset generator to train image-based AI models. Due to the hazardous environment of thunderstorms obtaining real data is extremely challenging.

Limitations and Future Work Our framework can be extended in multiple directions. First, we currently neglect the role of ion capture, aerosol particles, and other ice-ice collisions in the atmosphere. Modeling their microphysical effects would enable the simulation of weakly electrified clouds [19] and additional atmospheric discharges like St. Elmo's fire, as well as more precise measurements of ice nucleation and its impact on electrification, see Figure 10. Additionally, we assume that heat energy released by lightning is quickly dissipated in the atmosphere because of the spatio-temporal scales used in our simulations, and the fact that air is a poor heat conductor [3]. However, considering the thermodynamic coupling between lightning and air would open the possibility to study other breakdown phenomena e.g., Jacob's Ladder. Finally, it would be interesting to consider additional interactions with the ground, like the impact of lightning on wildfires through CG strikes, and the role of local charge induction, which generates a net charge at the ground that can trigger ground-to-cloud (GC) strikes.

8 Conclusion

We have introduced a novel physically-based model for the efficient and comprehensive simulation of emergent atmospheric lightning. Our multi-physics approach explicitly models and integrates cloud electrification at the microphysical level and the dielectric breakdown of air by parametrizing and coupling the underlying fluid-mechanics, thermodynamics, and electrodynamics responsible for atmospheric lightning. Our method represents a compromise between efficiency and physical complexity, which enables the interactive control and modeling over a large set of lightning phenomena which have not been simulated before.

Our scheme has been evaluated and validated by performing multiple experiments to compare to state-of-the-art and real data obtained from optical and radar technologies as well as local weather soundings. The

results of these experiments demonstrate that our framework improves the visual simulation of lightning and is able to reproduce results obtained from highly specialized engineering and atmospheric models. Moreover, we have simulated diverse types of complex atmospheric lightning as well as the life cycle of a thunderstorm, showing the capabilities of our framework to simulate and control emergent lightning from a reduced set of parameters. We have also explored diverse applications of our integrated framework, from real-time nowcasting and civil engineering measurements to generating virtual environments together with acoustic effects. Finally, we have shown additional uses of our discharge module EDS for simulating dielectric breakdown within complex domains while considering dynamic electric fields and electrical resistance.

Future work includes the modeling of additional phenomena, like ion capture and the presence of aerosol particles, as well as the thermodynamic coupling of lightning with the surrounding air. Finally, including more advanced ground interactions would also be an interesting path for future research.

Acknowledgements

This work has been partially funded by KAUST through the baseline funding of the Computational Sciences Group.

References

[1] J. A. Amador Herrera, T. Hädrich, W. Pałubicki, D. T. Banuti, S. Pirk, and D. L. Michels. Weatherscapes: Nowcasting heat transfer and water continuity. *ACM Transaction on Graphics*, 40(6), article no. 204, 12 2021.

[2] J. AmadorHerrera, J. Klein, D. Liu, W. Pałubicki, S. Pirk, and D. L. Michels. Cyclogenesis: Simulating hurricanes and tornadoes. *ACM Transaction on Graphics*, 43(4), article no. 71, 7 2024. doi: 10.1145/3658149

[3] S. Beirão, A. Ribeiro, M. Lourenço, F. Santos, and C. Nieto de Castro. Thermal conductivity of humid air. *International Journal of Thermophysics*, 33:1686–1703, 2012.

[4] A. Bouthors and F. Neyret. Modeling clouds shape. In M. Alexa and E. Galin, eds., *Eurographics 2004–Short Presentations*. Eurographics Association, 2004.

[5] M. Chandra. The effective role of ions and cloud microphysics in electrification of clouds. In *AIP Conference Proceedings*, vol. 2782. AIP Publishing, 2023.

[6] C.-S. Chiu. Numerical study of cloud electrification in an axisymmetric, time-dependent cloud model. *Journal of Geophysical Research: Oceans*, 83(C10):5025–5049, 1978.

[7] L. Coleman, T. Marshall, M. Stolzenburg, T. Hamlin, P. Krehbiel, W. Rison, and R. Thomas. Effects of charge and electrostatic potential on lightning propagation. *Journal of Geophysical Research: Atmospheres*, 108(D9), 2003.

[8] V. Cooray. *An introduction to lightning*, vol. 201. Springer, 2015.

[9] J. Delanoë, A. Protat, J. Testud, D. Bouniol, A. Heymsfield, A. Bansemer, P. Brown, and R. Forbes. Statistical properties of the normalized ice particle size distribution. *Journal of Geophysical Research: Atmospheres*, 110(D10), 2005.

[10] L. Dellera and E. Garbagnati. Lightning stroke simulation by means of the leader progression model. *IEEE Transactions on Power Delivery*, 1990.

[11] D. Demidov. Amgcl: An efficient, flexible, and extensible algebraic multigrid implementation. *Lobachevskii Journal of Mathematics*, 40(5):535–546, May 2019. doi: 10.1134/S1995080219050056

[12] Y. Dobashi, T. Yamamoto, and T. Nishita. Efficient rendering of lightning taking into account scattering effects due to clouds and atmospheric particles. In *Proceedings Ninth Pacific Conference on Computer Graphics and Applications. Pacific Graphics 2001*, pp. 390–399, 2001. doi: 10.1109/PCCGA.2001.962896

[13] C. W. Ferreira Barbosa, Y. Dobashi, and T. Yamamoto. Adaptive cloud simulation using position based fluids. *Comput. Animat. Virtual Worlds*, 26(3–4):367–375, 9 pages, 2015.

[14] I. Garcia-Dorado, D. G. Aliaga, S. Bhalachandran, P. Schmid, and D. Niyogi. Fast weather simulation for inverse procedural design of 3d urban models. *ACM Trans. Graph.*, 36(2), article no. Article 21, 19 pages, 2017.

[15] G. Y. Gardner. Visual simulation of clouds. In *Proceedings of the 12th Annual Conference on Computer Graphics and Interactive Techniques*, SIGGRAPH '85, 8 pages, pp. 297–304. Association for Computing Machinery, 1985.

[16] C. Gissler, A. Henne, S. Band, A. Peer, and M. Teschner. An implicit compressible sph solver for snow simulation. *ACM Trans. Graph.*, 39(4), article no. 36, 16 pages, 2020.

[17] P. Goswami and F. Neyret. Real-time landscape-size convective clouds simulation and rendering. In *Proceedings of the 13th Workshop on Virtual Reality Interactions and Physical Simulations*, VRIPHYS '17, 8 pages, pp. 1–8. Eurographics Association, 2017.

[18] E. J. Griffith, F. H. Post, T. Heus, and H. J. J. Jonker. Interactive simulation and visualisation of atmospheric large-eddy simulations. Technical report, Technical Report 2 TuDelft Data Visualization Group, 2009.

[19] R. Griffiths, J. Latham, and V. Myers. The ionic conductivity of electrified clouds. *Quarterly Journal of the Royal Meteorological Society*, 100(424):181–190, 1974.

[20] T. Hädrich, D. T. Banuti, W. Pałubicki, S. Pirk, and D. L. Michels. Fire in paradise: Mesoscale simulation of wildfires. *ACM Trans. on Graph.*, 40(4), article no. 163, 2021.

[21] T. Hädrich, M. Makowski, W. Pałubicki, D. T. Banuti, S. Pirk, and D. L. Michels. Stormscapes: Simulating cloud dynamics in the now. *ACM Transaction on Graphics*, 39(6), article no. 175, 12 2020.

[22] Y. Han, H. Luo, Y. Wu, Y. Zhang, and W. Dong. Cloud ice fraction governs lightning rate at a global scale. *Communications Earth & Environment*, 2(1):157, 2021.

[23] T. Hao. Thunderscapes: Simulating the dynamics of mesoscale convective system. *arXiv preprint arXiv:2412.00703*, 2024.

[24] M. J. Harris, W. V. Baxter, T. Scheuermann, and A. Lastra. Simulation of cloud dynamics on graphics hardware. In *ACM SIGGRAPH/EUROGRAPHICS Conference on Graphics Hardware*, HWWS '03, 10 pages, pp. 92–101. Eurographics Association, 2003.

[25] R. G. Harrison and G. J. Marlton. Fair weather electric field meter for atmospheric science platforms. *Journal of Electrostatics*, 107:103489, 2020.

[26] M. Hoffman. How to generate shockingly good 2d lightning effects, 2013.

[27] A. Houard, P. Walch, T. Produit, V. Moreno, B. Mahieu, A. Sunjerga, C. Herkommer, A. Mostajabi, U. Andral, Y.-B. André, M. Lozano, L. Bizet, M. C. Schroeder, G. Schimmel, M. Moret, M. Stanley, W. A. Rison, O. Maurice, B. Esmiller, K. Michel, W. Haas, T. Metzger, M. Rubinstein, F. Rachidi, V. Cooray, A. Mysyrowicz, J. Kasparian, and J.-P. Wolf. Laser-guided lightning. *Nature Photonics*, Jan 2023.

[28] R. Jiang, W. Lyu, B. Wu, Q. Qi, Y. Ma, Z. Su, S. Wu, Z. Xie, and Y. Tan. Simulation of cloud-to-ground lightning strikes to structures based on an improved stochastic lightning model. *Journal of Atmospheric and Solar-Terrestrial Physics*, 203:105274, 2020.

[29] J. T. Kajiya and B. P. Von Herzen. Ray tracing volume densities. *ACM SIGGRAPH computer graphics*, 18(3):165–174, 1984.

[30] T. Kim and M. Lin. Physically based animation and rendering of lightning. pp. 267–275, 11 2004.

[31] T. Kim and M. C. Lin. Visual simulation of ice crystal growth. In *Proceedings of the 2003 ACM SIGGRAPH/Eurographics symposium on Computer animation*, pp. 86–97. Citeseer, 2003.

[32] T. Kim and M. C. Lin. Fast animation of lightning using an adaptive mesh. *Transactions on Visualization and Computer Graphics*, 13(2), 2007.

[33] T. Kim, J. Sewall, A. Sud, and M. C. Lin. Fast simulation of laplacian growth. *IEEE computer graphics and applications*, 27(2):68–76, 2007.

[34] A. Kokosza, H. Wrede, D. Gonzalez Esparza, M. Makowski, D. Liu, D. L. Michels, S. Pirk, and W. Palubicki. Scintilla: Simulating combustible vegetation for wildfires. *ACM Transactions on Graphics (TOG)*, 43(4):1–21, 2024.

[35] P. K. Kundu, I. M. Cohen, and D. R. Dowling. Fluid mechanics, 5th version. *Academic, Berlin*, 2012.

[36] D. R. MacGorman, W. D. Rust, T. J. Schuur, M. I. Biggerstaff, J. M. Straka, C. L. Ziegler, E. R. Mansell, E. C. Bruning, K. M. Kuhlman, N. R. Lund, et al. Telex the thunderstorm electrification and lightning experiment. *Bulletin of the American Meteorological Society*, 89(7):997–1014, 2008.

[37] C. Mallick, U. Dutta, M. Bhowmik, G. M. Mohan, A. Hazra, R. Ghosh, S. Pawar, and J.-P. Chen. Comparison of two-moment and three-moment bulk microphysics schemes in thunderstorm simulations over indian subcontinent. *Atmospheric Research*, 310:107614, 2024.

[38] T. C. Marshall, M. P. McCarthy, and W. D. Rust. Electric field magnitudes and lightning initiation in thunderstorms. *Journal of Geophysical Research: Atmospheres*, 100(D4):7097–7103, 1995.

[39] R. Miyazaki, Y. Dobashi, and T. Nishita. Simulation of cumuliform clouds

based on computational fluid dynamics. In *Eurographics*, 2002.
[40] F. Neyret. Qualitative simulation of convective cloud formation and evolution. In *Computer Animation and Simulation '97*, pp. 113–124, 1997.
[41] L. Niemeyer, L. Pietronero, and H. J. Wiesmann. Fractal dimension of dielectric breakdown. *Physical Review Letters*, 52(12):1033, 1984.
[42] D. Overby, Z. Melek, and J. Keyser. Interactive physically-based cloud simulation. In *Proceedings of Pacific Graphics*, pp. 469–470, 2002.
[43] W. Pałubicki, M. Makowski, W. Gajda, T. Hädrich, D. L. Michels, and S. Pirk. Ecoclimates: Climate-response modeling of vegetation. *ACM Trans. Graph.*, 41(4), article no. 1, 19 pages, July 2022.
[44] P. C. Pretorius, J. Gain, M. Lastic, G. Cordonnier, J. Chen, D. Rohmer, and M.-P. Cani. Volcanic skies: coupling explosive eruptions with atmospheric simulation to create consistent skyscapes. In *Computer Graphics Forum*, vol. 43, p. e15034. Wiley Online Library, 2024.
[45] C. G. Price. Lightning applications in weather and climate research. *Surveys in Geophysics*, 34:755–767, 2013.
[46] X. Qie, Y. Pu, R. Jiang, Z. Sun, M. Liu, H. Zhang, X. Li, G. Lu, and Y. Tian. Bidirectional leader development in a preexisting channel as observed in rocket-triggered lightning flashes. *Journal of Geophysical Research: Atmospheres*, 122(2):586–599, 2017.
[47] W. Raateland, T. Hädrich, J. A. A. Herrera, D. T. Banuti, W. Pałubicki, S. Pirk, K. Hildebrandt, and D. L. Michels. Dcgrid: An adaptive grid structure for memory-constrained fluid simulation on the gpu. *Proc. ACM Comput. Graph. Interact. Tech.*, 5(1), article no. 3, 14 pages, May 2022.
[48] T. Reed and B. Wyvill. Visual simulation of lightning. In *Proceedings of the 21st Annual Conference on Computer Graphics and Interactive Techniques*, SIGGRAPH '94, 6 pages, pp. 359–364. Association for Computing Machinery, New York, NY, USA, 1994.
[49] R. V. Rohli, C. Li, R. V. Rohli, and C. Li. Lightning. *Meteorology for Coastal Scientists*, pp. 259–266, 2021.
[50] J. Schalkwijk, H. J. J. Jonker, A. P. Siebesma, and E. Van Meijgaard. Weather forecasting using gpu-based large-eddy simulations. *Bulletin of the American Meteorological Society*, 96(5):715–723, 2015.
[51] Z. Shi, L. Li, Y. Tan, H. Wang, and C. Li. A numerical study of aerosol effects on electrification with different intensity thunderclouds. *Atmosphere*, 10(9):508, 2019.
[52] T. Takahashi. Riming electrification as a charge generation mechanism in thunderstorms. *Journal of Atmospheric Sciences*, 35(8):1536–1548, 1978.
[53] Y. Tan, Z. Shi, Z. Chen, L. Peng, Y. Yang, X. Guo, and H. Chen. A numerical study of aerosol effects on electrification of thunderstorms. *Journal of Atmospheric and Solar-Terrestrial Physics*, 154:236–247, 2017.
[54] U. Vimont, J. Gain, M. Lastic, G. Cordonnier, B. Abiodun, and M.-C. Cani. Interactive meso-scale simulation of skyscapes. *Eurographics*, 2020.
[55] A. Webanck, Y. Cortial, E. Guérin, and E. Galin. Procedural cloudscapes. In *Computer Graphics Forum*, vol. 37, pp. 431–442. Wiley Online Library, 2018.
[56] J. Yang, S. Huang, T. Yang, Q. Zhang, Y. Deng, and Y. Liu. Impact of ice multiplication on the cloud electrification of a cold-season thunderstorm: a numerical case study. *Atmospheric Chemistry and Physics*, 24(10):5989–6010, 2024.
[57] L. Yu. Global variations in oceanic evaporation (1958–2005): The role of the changing wind speed. *Journal of climate*, 20(21):5376–5390, 2007.
[58] J. Yun, M. Son, B. Choi, T. Kim, and S.-E. Yoon. Physically inspired, interactive lightning generation. *Computer Animation and Virtual Worlds*, 2017.
[59] R. Zeng, C. Zhuang, X. Zhou, S. Chen, Z. Wang, Z. Yu, and J. He. Survey of recent progress on lightning and lightning protection research. *High Voltage*, 1(1):2–10, 2016.
[60] C. L. Ziegler, D. R. MacGorman, J. E. Dye, and P. S. Ray. A model evaluation of noninductive graupel-ice charging in the early electrification of a mountain thunderstorm. *Journal of Geophysical Research: Atmospheres*, 96(D7):12833–12855, 1991.

APPENDIX

A LIST OF SYMBOLS

We present a list of the symbols used in our model, and their corresponding values and units, in Table 2.

Table 2: List of different symbols (in order of appearance) used in our model and their typical values for simulation, where N.I. stands for "Non-Inductive". Note that quantities without a shown value correspond to dynamic parameters computed at simulation time.

Symbol	Name	Value	Units
$x = (x, y, z)$	Cartesian Coordinates	–	m
a	Dummy Index: Vapor v, Rain r, etc.	–	–
q_a	Mixing Ratio of a	–	$\mathrm{kg\,kg^{-1}}$
u	Wind Velocity	–	$\mathrm{m\,s^{-1}}$
Q_a	Charge of a	–	C
θ	Vapor Temperature	–	K
Φ	Electric Potential	–	V
T	Ambient Temperature	–	K
p	Ambient Pressure	–	Pa
$U_{a,b}$	Transfer of a into b	–	$\mathrm{kg\,kg^{-1}\,s^{-1}}$
$n_a(D)$	Number Density of Particles	–	$\mathrm{m^{-4}}$
n_{0g}	Graupel Intercept	4×10^4	$\mathrm{m^{-4}}$
n_{0s}	Snow Intercept	3×10^6	$\mathrm{m^{-4}}$
n_{0i}	Cloud Ice Intercept	2×10^6	$\mathrm{m^{-4}}$
n_{0r}	Rain Intercept	8×10^6	$\mathrm{m^{-4}}$
n_{0c}	Cloud Water Intercept	8×10^6	$\mathrm{m^{-4}}$
D_a	Characteristic Diameter	–	m
ρ_{air}	Air Density	1.29	$\mathrm{kg\,m^{-3}}$
ρ_g	Graupel Density	500	$\mathrm{kg\,m^{-3}}$
ρ_s	Snow Density	75	$\mathrm{kg\,m^{-3}}$
ρ_i	Cloud Ice Density	720	$\mathrm{kg\,m^{-3}}$
ρ_r	Rain Density	1000	$\mathrm{kg\,m^{-3}}$
$\sigma'_{b,g}$	N.I. Charge Transfer	–	C
$\sigma_{b,g}$	Bulk N.I. Charge Transfer	–	C
$C_{b,g}$	Collection Efficiency	–	1
E_z	Vertical Component of E	–	$\mathrm{NC^{-1}}$
$\tau_{w,g}$	Bulk Inductive Charge Transfer	–	C
$C_{w,g}$	Collision Efficiency	–	1
ε	Permittivity of Air	8.85×10^{-12}	$\mathrm{F\,m^{-1}}$
$\overline{\theta}$	Average Collision Angle	0.2	rad
C_r	Rebound Probability	0.007	1
ρ_Q	Volumetric Charge Density	–	$\mathrm{C\,m^{-3}}$
E	Electric Field	–	$\mathrm{NC^{-1}}$
E_0	Fair Weather Field	$-300\hat{z}$	$\mathrm{NC^{-1}}$
E_{break}	Breakdown Field	–	$\mathrm{NC^{-1}}$
E_{critic}	Critical Material Field	–	$\mathrm{NC^{-1}}$
η	Weighting Factor	1.0	1
s	Charge Polarity	–	1
E_{int}	Internal Field Resistance	–	$\mathrm{NC^{-1}}$
B_L	Flash Brightness	–	1
α_L	Brightness Constant	–	$\mathrm{C^{-1}}$
q_f	Ice Fraction	–	1

–Supplementary Material–
Thunderstruck: Visually Simulating Electrical Storms

Jorge Alejandro Amador Herrera, Jonathan Klein, Daniel T. Banuti,
Wojtek Pałubicki, Sören Pirk, Dominik L. Michels

1 Statistical Ensembles

Using our one-moment statistical approach for microphysics, we are able to compute *bulk* or average quantities associated to ice and water particles via integration over statistical ensembles. We show, as an example, the detailed computation of characteristic diameters.

Since we assume spherical particles for each species a, the mass $m_a(D)$ of a single particle with diameter D is given by

$$m_a(D) = \frac{4}{3}\pi\rho_a D^3\,,$$

where ρ_a is the density of a. Then, we integrate over an statistical ensemble of particles with diameters D to compute the *bulk* density $\overline{\rho_a}$ of the ensemble as

$$\begin{aligned}\overline{\rho_a} &= \int_0^\infty n_a(D) m_a(D)\, dD\,,\\ &= \frac{4}{3}\pi\rho_a n_{0a}\int_0^\infty D^3 \exp\left(-D/D_a\right) dD\,,\\ &= 8\pi\rho_a n_{0a} D_a^4\,.\end{aligned}$$

Moreover, by definition, the mass fraction or mixing ratio q_a is the mass of a per unit mass of dry air, so we have

$$q_a = \frac{\mathrm{M}_a}{\mathrm{M}_{\text{air}}} = \frac{\mathrm{M}_a/V}{\mathrm{M}_{\text{air}}/V} = \frac{\overline{\rho_a}}{\rho_{\text{air}}}\,,$$

where V is the volume where the particles are contained. Combining these two results we have

$$q_a = \frac{8\pi\rho_a n_{0a} D_a^4}{\rho_{\text{air}}}\,.$$

Solving for the characteristic diameter D_a we arrive at

$$D_a = \left(\frac{\rho_{\text{air}} q_a}{8\pi\rho_a n_{0a}}\right)^{1/4}\,,$$

which is Eq. 3 of our model. We are then able to compute additional *bulk* quantities in terms of the mass fraction q_a via integration.

2 Discharge Scheme Comparison

A detailed algorithmic comparison of PDS and our formulation with gauge-invariance and electrical resistance is presented in Table 1. In particular, note that we explicitly consider the electric resistance of both the material and the channel in the probability and potential update. Furthermore, since PDS uses the potential for promoting discharge growth, multiple polarities and negative potentials result in negative probabilities.

- *J.A. Amador Herrera, J. Klein, D.L. Michels are with KAUST. E-mail: {jorge.amadorherrera,jonathan.klein,dominik.michels}@kaust.edu.sa*
- *D.T. Banuti is with KIT. E-mail: danielbanuti@kit.edu*
- *W. Pałubicki is with AMU. E-mail: wp06@amu.edu.pl*
- *S. Pirk is with CAU. E-mail: sp@informatik.uni-kiel.de*

Table 1: Main algorithmic differences between PDS and our formulation EDS.

Feature	PDS	EDS
Probability Update	$\mathcal{N}\Phi^\eta$	$\mathcal{N}\left[E(k_c,k) - E_{\text{critic}}\right]^\eta$
Potential Update	$\Phi_{k_n} = \Phi_{k_c} = 0$	$\phi_{k_n} = \phi_{k_c} - s\left[h\gamma(k_c,k_n)\, E_{\text{int}}\right]$
Channel Resistance	–	E_{int}
Medium Resistance	–	E_{critic}
Polarity	Always Negative	s
Grid Size	–	$d(k_c,k_n)$

Additionally, the discharge channel must start at zero potential and be fixed at that value to avoid having a positive probability of self-intersection. For general fields, where discharges are usually triggered at points of $\Phi \neq 0$, a *gauge-transformation* $\Phi \to \Phi + C$ with constant C can be applied to the potential so that all probabilities become non-negative. This approach, however, does not always work, as demonstrated in Figure 1, and becomes more problematic when dealing with dynamic fields, as the particular gauge C that produces a non-negative potential should be adjusted per-frame. Note that, since we compute the probabilities using the electric field, which transforms as $E = -\nabla\Phi \to E' = -\nabla(\Phi + C) = -\nabla\Phi = E$ under a gauge chance, our approach is automatically *gauge-invariant* i.e., it produces non-negative probabilities regardless of the chosen gauge C or dynamic changes in the field.

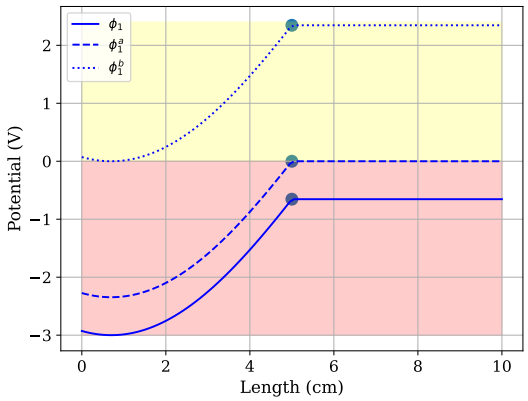

Fig. 1: Example of a discharge in a 1D potential ϕ_1 using PDS. For a discharge triggered at $x = 5$ cm, all probabilities would be negative. We can adjust the gauge to ϕ_1^a so that lightning starts at zero potential, but half of the probabilities are still negative, and the other half are zero. A third gauge can be used to get a positive potential ϕ_1^b that produces positive probabilities, but now lightning can self-intersect.

3 Complex Discharges

We present several use cases of our discharge framework EDS for simulating channels under complex domains, including dynamic electric fields, multiple polarities, as well as medium and channel resistance.

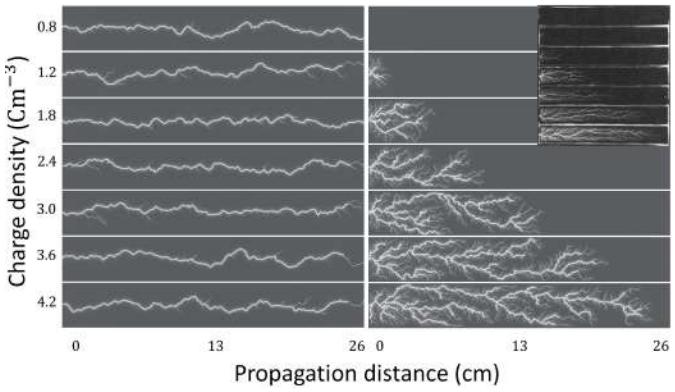

Fig. 2: Simulation of dielectric breakdown in plastic based on the experimental setup of Williams et. al. [6] (top corner) using PDS (left) and EDS (right). Considering the field intensity and material resistance in our scheme enables us to reproduce the correlation between charge density and propagation distance of each discharge.

3.1 Dielectric Materials

We reproduce the experiment of Williams et. al. [6] for dielectric breakdown of charged plastic slabs, as demonstrated in Figure 2. Since we take into account the material resistance and field intensity, the correlation between charge density and propagation distance to capture correctly the dielectric breakdown with different charge density values. In contrast, PDS promotes lightning channel growth to all zones of positive potential, so all channels reach the end of the slab regardless of the field intensity - which does not conform to observations of reality.

3.2 Dynamical Fields

In Figure 3 we show the simulation of dielectric breakdown between charged diodes using PDS and our approach. In our model, changes in the dynamical electric field are reflected on the automatic trigger and termination of the discharge with varying diode distances. In contrast, PDS generates a single channel between fixed prescribed points which incorrectly does not terminate with increasing diode distance.

Furthermore, we simulate a *plasma ball* using both methods, as demonstrated in Figure 5. The multiple channel and dynamical field considerations of our extended scheme enable us to reproduce the emergence of characteristic electric filaments from the center electrode towards the glass exterior (Fig. 5, top left). EDS correctly describes the arrest of the filaments when a conductor touches the boundary of the domain (Fig. 5, bottom left). In contrast, PDS can only produce a single sustained arc by prescribing the end-points of the discharge, but is not able to capture the filaments.

3.3 Local Maxima

One important challenge in PDS is that this scheme tends to promote lightning channel growth towards local maxima of the potential, which results in overgrowth within complex geometries. This is usually addressed by adding intermediate *way-points* that are positively charged and guide the channel towards its final destination [7], but such an approach requires additional user input, and can become impractical for more complex thunderstorm scenarios.

In comparison, EDS inherently prevents overgrowth. Specifically, EDS discards points for which the field intensity does not exceed the threshold imposed by the material resistance. PDS considers these points, leading to unrealistic overgrowth towards local maxima. This is demonstrated in Figure 4, where we compare the discharge within a complex domain using PDS and our scheme.

4 Thunder Simulation

Each time a discharge is triggered, we extract the relevant physical quantities from our simulator and use them as input for computing the associated thunder.

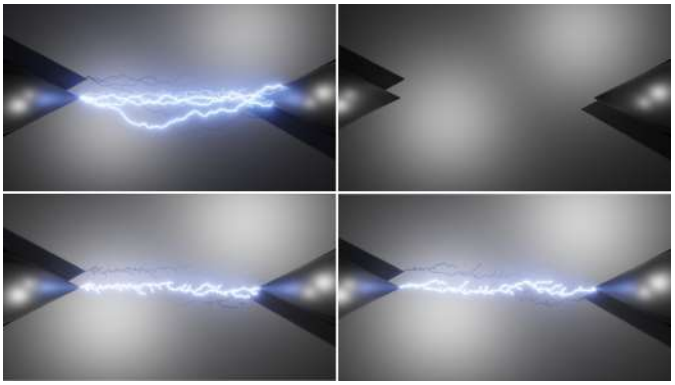

Fig. 3: Sustained arc between two diodes simulated using EDS (top) and PDS (bottom). Both diodes are increasingly charged until a sustained electric arc is established between them (left). When the diodes are moved apart, the strength of the field decreases (right). EDS reflects dynamical changes on the underlying electric field, while PDS produces only one channel between fixed prescribed points.

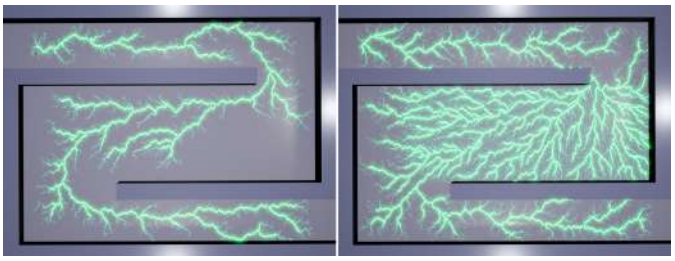

Fig. 4: Discharges within a complex domain simulated using PDS (left) and EDS (right). Overgrowth is automatically prevented in our formulation because we discard points (based on field intensity and material resistance) that would be considered in PDS to promote channel growth. In this case, PDS took 93,237 steps to reach the end of the domain due to overgrowing, while EDS took only 20,636 steps.

4.1 Point Audio Source Center

First, we reduce the lightning to a single point audio source by integrating over the volume of the channel V to retrieve the average point

$$x = \left(\int_{y \in V} \frac{Q_y}{\|y - x_O\|} \, \mathrm{d}y \right)^{-1} \int_{y \in V} \frac{Q_y}{\|y - x_O\|} x_v \, \mathrm{d}y \,, \tag{1}$$

where $Q = \int_{y \in V} Q_y \, \mathrm{d}y$ is the net charge, and x_O the observer position. Then, we average the atmospheric quantities along the connection path L between x and x_O, and obtain the temperature $T = \int_{v \in L} T_v \, \mathrm{d}v / \|L\|$, pressure $\rho = \int_{v \in L} \rho_v \, \mathrm{d}v / \|L\|$, and the relative humidity $h_r = \int_{v \in L} h_v \, \mathrm{d}v / \|L\|$, where $\|L\| = \|x - x_O\|$ measures the distance to the observer.

4.2 Delay

The delay $t_\Delta = c_{T,\rho} \|L\|$ between lightning and thunder is computed from the distance to the observer and the speed of sound, which, in general, depends on the temperature and pressure of the air [5] and is computed along the connection path according to

$$c_{T,\rho} = 20.05 \sqrt{1 + 0.4 \ln^2 \left(351.55 \, T / \rho \right)} / \sqrt{T} \,. \tag{2}$$

4.3 Volume

We determine the volume α of the thunder by considering both the net lightning charge and the distance to the listener. Therefore, we compute α as the sum of the power attenuation $\alpha_p = 10 \log_{10} \left(Q / Q_r \right)$, and the distance attenuation $\alpha_d = -6 \log_2 \left(\|L\| / \|L\|_r \right)$, where $\|L\|_r$ is the estimated distance of the sample lightning.

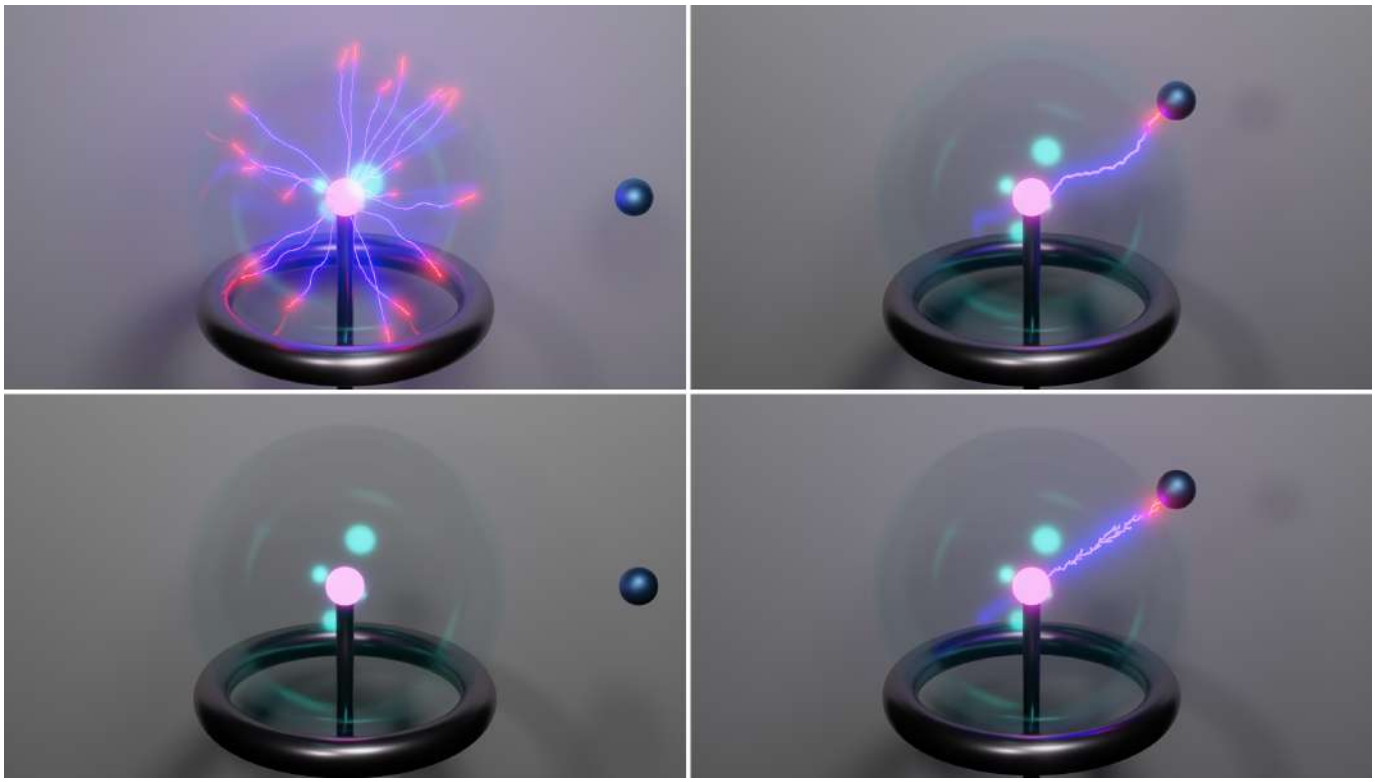

Fig. 5: *Plasma ball* simulated using EDS (top) and PDS (bottom). Our scheme is able to produce multiple electric filaments when the central electrode is charged (left) as well as the dynamical change produced when a conductor is moved towards the boundary (right), while PDS can produce the sustained arc by prescribing the end-points of the channel, but not the filaments as it does not support multiple channels nor dynamical fields.

4.4 Panning

Unequally distributing the sound across the left and right speaker creates a 3D panning effect. We compute the panning value $\chi = (\pi/2 - \arctan 2\,(y,x)) \,/\, (2\pi)$ as the angle between the view direction of the observer and the connection to the lightning position by mapping a 45° angle to the extreme *left/right* values; which effectively distributes the signal between the left ($\chi = -1$) and right ($\chi = 1$) speaker.

4.5 Frequency Adjustment

As the thunder travels through the air, its sound is affected by local atmospheric conditions; in particular, different frequencies of the sound are attenuated in different degrees [1–4]. We consider the saturation vapor pressure $\rho_s = -6.83 \cdot (T_{01}/T)^{1.261} + 4.62$, the molar concentration of water vapor $h = h_r \rho_s / \rho$, the relaxation frequency of molecular oxygen $f_O = \rho_s (24 + 40400h\,(0.02+h)(0.391+h)^{-1})$ [2], and the relaxation frequency of molecular nitrogen

$$f_N = \rho_s \sqrt{T_0/T} \left[9 + 280h \exp\left(-4.17 \left((T_o/T)^{1/3} - 1 \right) \right) \right]. \qquad (3)$$

The attenuation for each frequency f (in dB) is then computed as

$$\alpha_f = (f/\rho_s)^2 \tilde{k}\,(\|L\| - \|L_r\|) \left[1.84 \cdot 10^{-11} \,(T/T_O)^{1/2} + (T/T_O)^{-5/2} \right.$$
$$\left. \cdot \left(\frac{0.01278 \exp\left(-2239.1/T\right)}{f_O/\rho_s + (f/\rho_s)^2 \,/\, (f_O/\rho_s)} + \frac{0.10680 \exp\left(-3352.0/T\right)}{f_N/\rho_s + (f/\rho_s)^2 \,/\, (f_N/\rho_s)} \right) \right]$$

with $\tilde{k} = 8.69$ adapted from Eq. (3) of Bass et al. [3].

References

[1] H. E. Bass. The propagation of thunder through the atmosphere. *J. Acoust. Soc. Am.*, 1980. 3

[2] H. E. Bass, L. C. Sutherland, and A. J. Zuckerwar. Atmospheric absorption of sound: Update. *J. Acoust. Soc. Am.*, 1990. 3

[3] H. E. Bass, L. C. Sutherland, A. J. Zuckerwar, D. T. Blackstock, and D. M. Hester. Atmospheric absorption of sound: Further developments. *J. Acoust. Soc. Am.*, 1994. 3

[4] B. L. Evans, H. E. Bass, and L. C. Sutherland. Atmospheric absorption of sound: Theoretical predictions. *J. Acoust. Soc. Am.*, 1971. 3

[5] V. Kirtskhalia. The dependence of the speed of sound in the earth's atmosphereon its density and the correction of mach's number. *IOP Conf. Ser.: Mater. Sci. Eng.*, 2021. 2

[6] E. R. Williams, C. M. Cooke, and K. A. Wright. Electrical discharge propagation in and around space charge clouds. *Journal of Geophysical Research: Atmospheres*, 90(D4):6059–6070, 1985. 2

[7] J. Yun, M. Son, B. Choi, T. Kim, and S.-E. Yoon. Physically inspired, interactive lightning generation. *Computer Animation and Virtual Worlds*, 2017. 2